Structural and electronic properties of Cs(Pd(dmit)$_2$)$_2$

Structural and electronic properties of Cs[Pd(dmit)$_2$]$_2$

A E Underhill†, R A Clark†, I Marsden‡, M Allan‡, R H Friend‡,
H Tajima§, T Naito§, M Tamura§, H Kuroda§, A Kobayashi§,
H Kobayashi‖, E Canadell¶, S Ravy* and J P Pouget*

† Department of Chemistry, University College of North Wales, Bangor, Gwynedd
LL57 2UW, UK
‡ Cavendish Laboratory, Madingley Road, Cambridge CB3 0HE, UK
§ Department of Chemistry, Faculty of Science, University of Tokyo, Hongo, Bunkyo-ku, Tokyo 113, Japan
‖ Department of Chemistry, Faculty of Science, Toho University, Funabashi, Chiba 274, Japan
¶ Laboratoire de Chimie Théorique, Bâtiment 490, Université Paris-Sud, 91405 Orsay, France
* Laboratoire de Physique des Solides Associé au CNRS (LA2), Bâtiment 510, Université Paris-Sud, 91405 Orsay, France

Abstract. We report a series of measurements of the structural and electronic properties of the molecular conductor Cs[Pd(dmit)$_2$]$_2$ (dmit = isotrithionedithiolate). This material has a $C2/c$ structure with stacks of the acceptor groups arranged in sheets separated by the cations, with appreciable dimerization of the acceptor groups along the stack direction. It shows metallic properties at room temperature. We have characterized this material with measurements of conductivity, thermopower, magnetic susceptibility and polarized optical reflectivity, and we find that the electronic structure is quite isotropic in the plane of the acceptor sheets. On cooling, there is a metal–insulator transition at 56.5 K, and this opens an energy gap at the Fermi energy. This transition is associated with a complex periodic lattice distortion comprising an incommensurate modulation and also a commensurate distortion, which breaks the C centring symmetry. We present a calculation of the electronic band structure using an extended Hückel formalism, and show that, owing to the strong dimerization along the stack direction, the Fermi energy lies halfway in a band of highest occupied molecular orbital character. We consider also how the observed structural instability is able to produce an energy gap over the whole Fermi surface, and propose a model that requires coupling between the two types of modulation.

1. Introduction

The molecular charge-transfer salts formed with M(dmit)$_2$ (dmit = isotrithione-dithiolate) are in many ways comparable to those formed with organic donor molecules such as TMTSF and BEDT-TTF, with intermolecular delocalization of the π-electron system, and a wide range of metallic behaviour. The M(dmit)$_2$ complex is shown schematically in figure 1; the usual choice for the metal atom are Ni, Pd or Pt. Much of the interest has been directed to complexes formed with TTF, usually of stoichiometry TTF[M(dmit)$_2$]$_2$, since the discovery of superconductivity in some of these materials. This was found

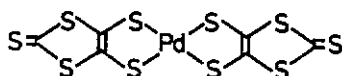Figure 1. Structure of Pd(dmit)$_2$ complex.

initially in TTF[Ni(dmit)$_2$]$_2$, which had a critical temperature T_c of 1.6 K at a pressure of 7 kbar[1–3]. A higher value of T_c has now been found in the α' phase of TTF[Pd(dmit)$_2$]$_2$, with T_c of 6.5 K at 20 kbar [4, 5].

It is also possible to make charge-transfer salts with closed-shell monovalent cations, including the alkali-metal ions and a wide range of substituted ammonium and phosphonium ions [6–11]. These materials can often be formed with stoichiometry X[M(dmit)$_2$]$_2$, though there are many reports of materials with lower molar fractions of the cation [12, 13]. Among these $(CH_3)_4$N[Ni(dmit)$_2$]$_2$ is of particular interest in that it shows superconducting behaviour, with a value of T_c of 5 K under an applied pressure of 7 kbar[14, 15]. More clearly than for salts formed with TTF, metallic and superconducting behaviour for these salts is associated with delocalization between the acceptor molecules. In this paper we present a comprehensive range of measurements we have made on Cs[Pd(dmit)$_2$]$_2$ [16]. This salt is similar in structure to $(CH_3)_4$N[Ni(dmit)$_2$]$_2$. However, as we show in the paper, though the Cs salt is metallic at room temperature, it undergoes a metal-to-insulator transition at 56.5 K at ambient pressure, and we were not able to suppress this transition under applied hydrostatic pressure of up to 10 kbar.

Most of the M(dmit)$_2$ salts investigated have structures with stacks of the M(dmit)$_2$ molecules, which can be expected to provide the best conducting direction in the crystal. The electronic structure of the M(dmit)$_2$ salts has been considered by Kobayashi *et al* [17] and by Canadell *et al* [18]. In spite of the large number of sulphur atoms on the periphery of the M(dmit)$_2$ molecule, which might be expected to give good contact between the M(dmit)$_2$ molecules on adjacent stacks, it is found in the α-TTF[M(dmit)$_2$]$_2$ (M = Ni, Pd) and Me$_4$N)[Ni(dmit)$_2$]$_2$ salts that these interactions are not particularly strong, and that these materials do show one-dimensional electronic structure. Evidence for charge-density-wave (CDW) formation driven by the $2k_F$ instability of the electron gas has been found in α-TTF[M(dmit)$_2$]$_2$ (M = Ni, Pd) [19]. However, as pointed out previously [18], the strength of the inter-stack interactions depends subtly on the interaction geometry, and can be quite strong. For instance, in the case of δ-TTF[Pd(dmit)$_2$]$_2$, inter-stack interactions were calculated to be stronger than intra-stack interactions [18]. No evidence for a $2k_F$ instability has been obtained to date for this phase [20]. As we show in this paper, Cs[Pd(dmit)$_2$]$_2$ is a new material that shows strong inter-stack interactions, but at the same time undergoes a structural phase transition driven by the instability of the low-dimensional electron gas.

2. Preparation

Cs[Pd(dmit)$_2$]$_2$ was obtained as well formed black plates, or as needle-like crystals, on the anode by electrocrystallization of CH_3CN (120 cm^3) containing (Bu$_4$N)$_2$[Pd(dmit)$_2$] (0.2 mmol) and CsPF$_6$ (5 mmol) using Pt wire electrodes and a current density of about 6 μA cm^{-2}. Crystals were grown on the anode for a period of about 7 days.
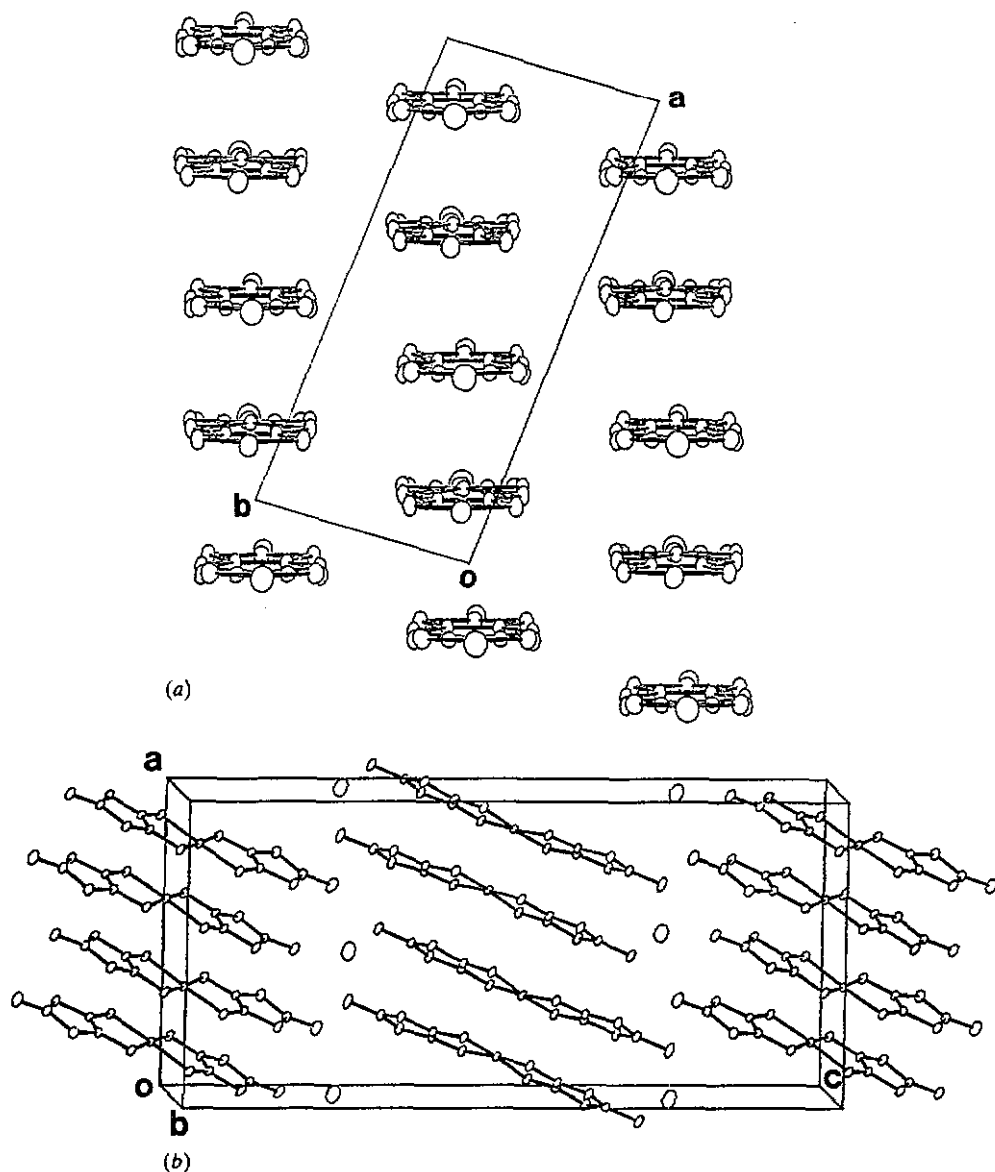
(a)

(b)

Figure 2. Crystal structure of Cs[Pd(dmit)₂]₂, (a) as viewed along the c axis, showing one of the anion slabs, and (b) projection showing alternation of stacking within slabs along the c axis.

3. Structure

The full structure was obtained by collection of 3443 independent reflections on a Rigaku automatic four-circle diffractometer with $|F_0| > 3\sigma(|F_0|)$ ($2\theta < 60°$, Mo K_α). The structure is monoclinic, $C2/c$, $a = 14.490(4)$, $b = 6.2629(14)$ and $c = 30.601(7)$ Å, $\beta = 90.58(2)°$, $V = 2777.02$ Å^3, $Z = 4$, and the final R value was 0.062. The crystal structure as viewed along c is shown in figure 2(a). As with other charge-transfer salts of this type,
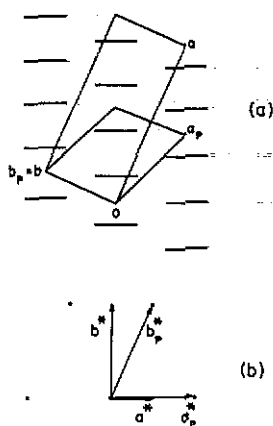
Figure 3. Diagram showing the relation between the centred (a, b) and primitive (a_p^*, b_p^*) lattices for a Pd(dmit)$_2$ slab in (a) real space and (b) reciprocal space.

the Pd(dmit)$_2$ anions form stacks, along the [110] direction in figure 2(a), which form sheets in the ab plane separated from one another by the Cs cations. There are two layers of each species per unit cell, which are related by a c glide plane symmetry so that the Pd(dmit)$_2$ anions of each slab are stacked along [110] and [$\bar{1}$10], in alternate sheets along [001]; see figure 2(b). These columns have periodicity of four molecules (see figure 2). However, as shown in figure 3(a), because the lattice is C-centred, the real repeat unit of the slab contains two anions.

Along the stacks, there is strong dimerization of the Pd(dmit)$_2$ anions, with an inter-dimer separation of 3.762 Å, as illustrated in figure 4. The Pd atoms of the dimers are displaced towards each other by 0.08 Å from the ligand plane formed by S1, S2, S3 and S4. Furthermore, as shown in figure 5, the Pd(dmit)$_2$ anions within the dimer pair are eclipsed, in contrast to the case of (CH$_3$)$_4$N[Ni(dmit)$_2$]$_2$, for which the anions are slipped sideways. This organization of the two anions clearly allows interaction between the d orbitals of the metal atoms, and it is well established that the strength of this interaction is in the order Ni < Pd < Pt [21]. Thus, the change from eclipsed to slipped packing from Cs[Pd(dmit)$_2$]$_2$ to (CH$_3$)$_4$N[Ni(dmit)$_2$]$_2$ follows the expected trend. The very much stronger dimerization in the Cs[Pd(dmit)$_2$]$_2$ salt has important consequences for the electronic structure, which we discuss in section 4.

Details of the atomic positions within the unit cell are shown in table 1. The Cs$^+$ cations occupy channels in the b direction and each is surrounded by six S atoms at distances of 3.589(3), 3.636(2) and 3.796(2) Å. Details of the shortest intermolecular sulphur-to-sulphur contacts are shown in table 2.

4. Electronic structure

The electronic structure of the Pd(dmit)$_2$ slabs in the Cs[Pd(dmit)$_2$]$_2$ salt was studied by means of molecular and tight-binding band-structure calculations [22] using an extended Hückel Hamiltonian [23], and a modified Wolfsberg–Helmholz formula to calculate the off-diagonal H_{ij} values [24]. The basis set and parameters used were taken from previous work on the TTF[Pd(dmit)$_2$]$_2$ salts [18].

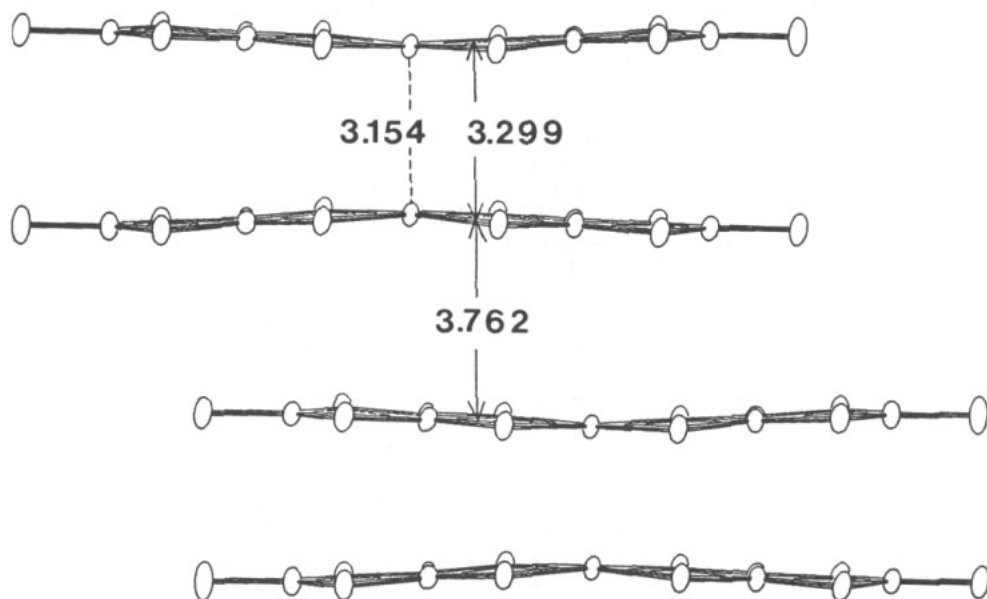**Figure 4.** Intra- and inter-dimer separation in Cs[Pd(dmit)₂]₂.

One of the interesting features of the Pd(dmit)₂ system is that its highest occupied (HOMO) and lowest unoccupied (LUMO) molecular orbitals are quite close in energy ($\simeq 0.4$ eV). The reasons behind this have been analysed in some detail elsewhere [18]. These orbitals are mainly ligand in character and are schematically shown in figure 6. In consequence, if there is dimerization of the Pd(dmit)₂ molecules, the splitting between the two combinations originating from each of these two orbitals can be large enough to

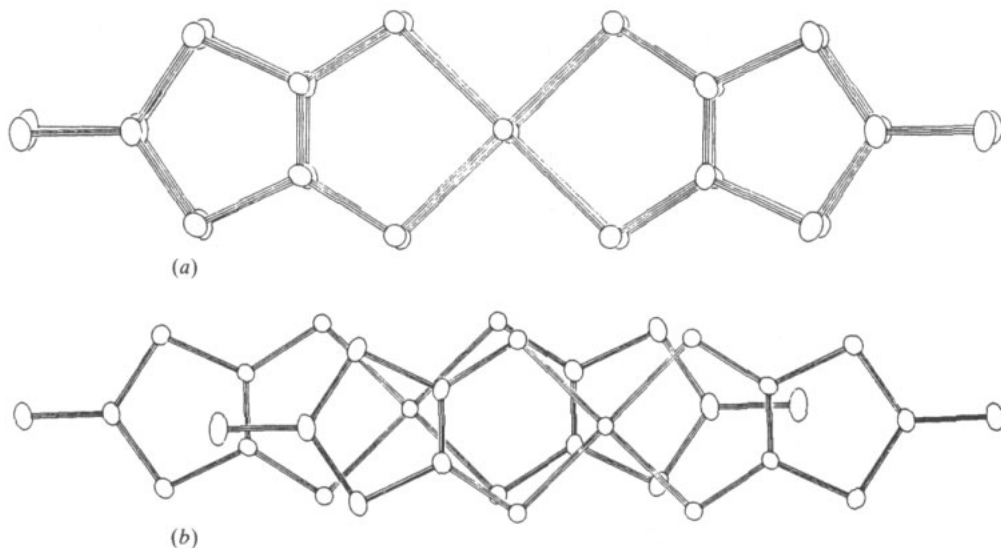**Figure 5.** (*a*) Intra- and (*b*) inter-dimer overlap in Cs[Pd(dmit)₂]₂.

A E Underhill et al

Table 1. Fractional atomic coordinates ($\times 10^5$) for $Cs[Pd(dmit)_2]_2$.

N	Atom	X	Y	Z
1	Cs	0	39 084(13)	25.000
2	Pd	84 461(2)	17 795(6)	52 123(1)
3	S1	92 852(10)	34 504(20)	46 824(4)
4	S2	84 990(10)	−13 369(20)	48 192(4)
5	S3	84 867(10)	48 573(20)	56 193(4)
6	S4	76 920(9)	670(20)	57 696(4)
7	S5	100 395(10)	18 947(21)	38 384(5)
8	S6	93 525(10)	−23 730(21)	39 554(4)
9	S7	78 591(11)	57 933(24)	65 317(5)
10	S8	71 539(11)	15 308(25)	66 580(5)
11	S9	103 314(12)	−12 436(28)	31 361(5)
12	S10	68 806(18)	47 431(36)	73 527(6)
13	C1	94 353(34)	14 724(77)	43 168(16)
14	C2	90 995(34)	−5901(75)	43 721(15)
15	C3	79 914(35)	40 516(80)	60 925(15)
16	C4	76 435(35)	20 190(83)	61 521(16)
17	C5	99 159(36)	−6064(87)	36 171(16)
18	C6	72 758(43)	40 602(106)	68 750(18)

Table 2. Short sulphur-to-sulphur contacts (<3.7 Å) in $Cs[Pd(dmit)_2]_2$.

Contact[a]	Distance (Å)
S1 . . . S2[i]	3.484(2)
S1 . . . S1[ii]	3.429(2)
S1 . . . S3[ii]	3.530(2)
S1 . . . S4[iii]	3.302(2)
S2 . . . S2[iv]	3.434(2)
S2 . . . S3[iii]	3.295(2)
S2 . . . S4[iv]	3.409(2)
S3 . . . S5[ii]	3.374(2)
S4 . . . S7[v]	3.557(2)
S4 . . . S6[v]	3.519(2)
S5 . . . S7[ii]	3.567(2)
S5 . . . S8[iii]	3.645(2)
S6 . . . S7[iii]	3.657(2)
S8 . . . S9[vi]	3.696(3)
S8 . . . S10[vii]	3.506(3)
S9 . . . S10[viii]	3.432(3)
S9 . . . S10[iii]	3.647(3)

[a] Symmetry codes:
i $\quad x, y + 1, z$;
ii $\quad 2 - x, 1 - y, 1 - z$;
iii $3/2 - x, 1/2 - y, 1 - z$;
iv $\quad 3/2 - x, -1/2 - y, 1 - z$;
v $\quad x, -1 + y, z$;
vi $\quad 2 - x, -7, 1 - z$;
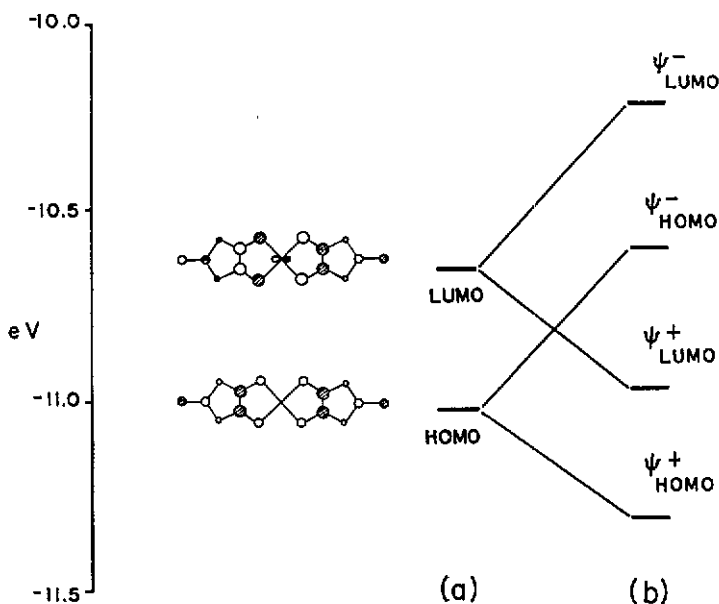vii $3/2 - x, y - 1/2, 3/2 - z$;
viii $1/2 - x, 1/2 - y, z - 1/2$.

Figure 6. HOMO and LUMO energy levels of a Pd(dmit)₂ monomer and dimer as found in the room-temperature structure of Cs[Pd(dmit)₂]₂.

raise the antibonding combination of the HOMO (Ψ^-_{HOMO}) above the bonding combination of the LUMO (Ψ^+_{LUMO}). As shown in figure 6 this is what happens in the case of Cs[Pd(dmit)₂]₂. Since the orbitals indicated in figure 6 are filled with five electrons, the singly occupied orbital of each Pd(dmit)₂ dimer is built from the HOMO of the monomer, rather than from the LUMO as could be expected from the acceptor character of Cs[Pd(dmit)₂]₂.

The repeat unit of each Cs[Pd(dmit)₂]₂ slab contains two monomers if we consider a primitive lattice defined by $a_p = (a - b)/2$ and $b_p = b$, where a and b are the lattice parameters of the monoclinic structure, as is illustrated in figure 3(a). The dispersion relations for the HOMO and LUMO bands of a Pd(dmit)₂ slab, as found in the room-temperature structure of Cs[Pd(dmit)₂]₂, are shown in figure 7. The nature of the four bands corresponds directly to the molecular orbitals of the dimeric unit shown in figure 6. In consequence, the half-filled band of these slabs originates from the HOMO of the
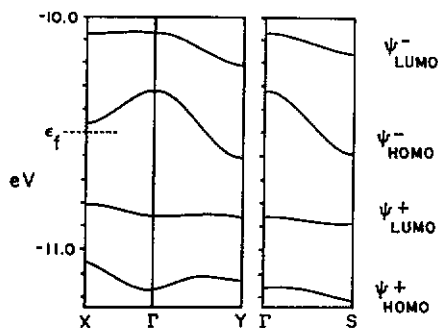
Figure 7. Dispersion relations for the HOMO and LUMO bands of the Pd(dmit)₂ slabs in Cs[Pd(dmit)₂]₂. Γ, X, Y and S represent the wavevectors $(0,0)$, $(a_p^*/2, 0)$, $(0, b_p^*/2)$ and $(-a_p^*/2, b_p^*/2)$ respectively, where a_p^* and b_p^* are the primitive wavevectors of the slab defined in figure 3.

Pd(dmit)$_2$. This apparently surprising feature was also noticed for δ-TTF[Pd(dmit)$_2$]$_2$ [18]. In contrast, the partially filled level of the related salt (CH$_3$)$_4$N[Ni(dmit)$_2$]$_2$ was found to originate from the LUMO of the acceptor. The origin of this change in the nature of the conduction band has been discussed elsewhere [25].

The partially filled band in figure 7 shows dispersion along $\Gamma \rightarrow$ X and $\Gamma \rightarrow$ Y and $\Gamma \rightarrow$ S, which are different inter-stack directions. However, the dispersion along $\Gamma \rightarrow$ X is clearly smaller and this leads to the open Fermi surface of figure 8(a) (full curve). As there is no equivalence between the b_p and $(a_\mathrm{p} - b_\mathrm{p})/2$ intra-slab directions, the dispersion is different along the $\Gamma \rightarrow$ Y and $\Gamma \rightarrow$ S reciprocal directions (figure 7) and the Fermi surface of figure 8(a) has no mirror symmetry.

The calculation just outlined uses a single-ζ basis for the C and S atoms. Since it has been claimed that double-ζ basis sets can be needed to describe systems with non-negligible inter-stack interactions [26], we have therefore performed such calculations here. In a double-ζ basis set each C and S orbital is represented as a combination of a diffuse and a contracted orbital and provides increased intermolecular overlap over that given by the single-ζ basis set [27]. Our calculations do indeed show an increase in intermolecular interaction, with the splitting between the Ψ^+ and Ψ^- combinations of both the HOMO and LUMO about twice ($\approx$1.4 eV) that of the single-ζ calculations shown in figure 6. Since with the new basis set the initial splitting between the HOMO and LUMO is also doubled, the bonding scheme of figure 6 remains qualitatively unchanged. In addition, the Fermi surface computed with the new basis set shows only minor changes, as shown by the broken curves in figure 8(a). Thus, as is often the case, the absolute value of the transfer integrals depends on the choice of the basis set, but the relative anisotropy does not, and the conclusions of the present section are not basis-set-dependent. The size of the transfer integrals can be fixed empirically to experiment, and we discuss this in relation to the optical properties in section 6.

A common feature of the Fermi surfaces of figure 8(a) is that they are open along the a^* direction. A similar situation was recently found [18] for δ-TTF[Pd(dmit)$_2$]$_2$. In the present case it is worth mentioning that the X point lies in a minimum of the dispersion along this direction and very near to the Fermi level (i.e. 0.04 eV above it). Thus, a slight perturbation to the calculated dispersion relations could result in the lifting of this band

(a)   (b)

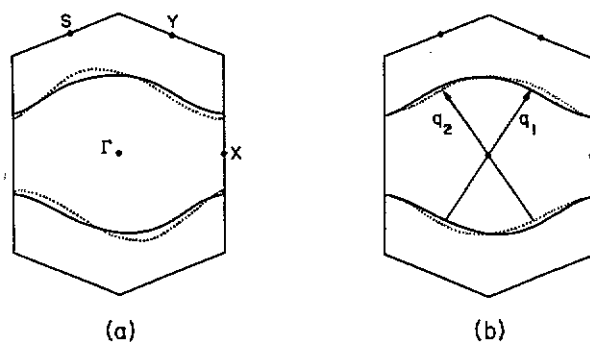Figure 8. (a) Fermi surface of the half-filled band of figure 7 (full curves for single-ζ calculation, dotted curves for double-ζ calculation). The Fermi energy contours separate unfilled states around Γ and X from filled states. (b) Superposition of the single-ζ Fermi surfaces due to the two Pd(dmit)$_2$ slabs related by the c glide plane. q_1 and q_2 are their nesting wavevectors.

above the Fermi energy at X, and thus cause the Fermi surface to be closed. Since the dispersion along the $\Gamma \rightarrow$ Y and $\Gamma \rightarrow$ S directions, although not identical, is quite similar, only a small area of the Fermi surface (i.e. around the X point) will be drastically changed as a result of such a perturbation. Interestingly, during the sudden change from open to closed Fermi surface, the X point would become the locus of a van Hove singularity in the density of states.

The real monoclinic $C2/c$ unit cell contains two Pd(dmit)₂ slabs related by the c glide plane symmetry. The true Fermi surface must possess the $2/m$ symmetry of the monoclinic Brillouin zone. If we ignore the tunnelling interaction between the slabs, the Fermi surface of the material is just the superposition of the Fermi surface shown in figure 8(a) (either the single-ζ or the double-ζ surface) and that related by the [010] mirror symmetry (see figure 8(b) for the single-ζ surface). For one slab the upper and lower parts of the Fermi surface calculated with the single-ζ basis set can be rather well nested by the wavevector $q \simeq 0.16a_p^* + 0.55b_p^*$. Since the real crystal contains two slabs per unit cell related by a c glide plane symmetry, there are two different nesting wavevectors, each associated with a particular slab: $q_1 = 0.87a^* + 0.55b^*$ and $q_2 = 1.13a^* + 0.55b^*$. The nesting wavevectors for the double-ζ Fermi surface are similar: $q_1 = 0.88a^* + 0.48b^*$ and $q_2 = 1.12a^* + 0.48b^*$. The correspondence between the (a_p^*, b_p^*) and (a^*, b^*) reciprocal wavevectors is shown in figure 3(b). As discussed in section 7, the system undergoes a distortion at low temperatures with mean wavevector of $q = a^* + 0.48b^* (= a^* + \frac{1}{2}(1 - \delta)b^*)$. We defer further discussion of these results to section 8.

5. Transport and magnetic properties

5.1. Experimental details

Electrical contacts were made with 10 μm gold wire attached to evaporated gold pads with silver paste, and with a contact geometry that gives measurements of the in-plane resistivity. Details of the low-frequency AC measurement have been reported previously [28]. Measurements at pressures up to 10 kbar were performed with beryllium–copper pressure cell in communication with a large intensifier/pressure reservoir, which remains at room temperature, via a stainless-steel capillary tube. This system allows accurate control of pressure down to the freezing point of the pentane used as the high-pressure medium (120 K at ambient pressure), and shows little pressure variation below the freezing point [29]. It does not, therefore, suffer from the considerable pressure losses with cooling usually encountered with 'clamp' cells, and provides a particularly convenient system for the present set of measurements. Measurements at higher pressures were performed with a Maraging steel clamp cell of conventional design.

Thermopower was measured by thermally anchoring the crystal to two gold-coated copper blocks, which could be separately heated to typically 1 K above the ambient temperature in the sample space of the cryostat. The thermovoltages developed across the sample and also across a differential thermocouple of rhodium +0.5% iron versus chromel [29] were measured with nanovoltmeters.

The magnetic susceptibility was measured using a Faraday balance, in fields of 0.77 and 0.87 T and over the temperature range 5 to 300 K. A randomly oriented collection of small crystals (of total mass 12 mg) was measured. Correction for ferromagnetic impurities was made using a Honda–Owen analysis of the field dependence of the susceptibility, and the experimental results are corrected for 8.3 ppm equivalent iron.
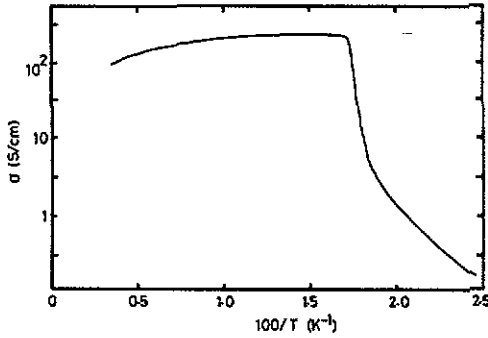
Figure 9. Log of conductivity versus reciprocal temperature, measured in the *ab* plane.

5.2. Results

$Cs[Pd(dmit)_2]_2$ is metallic at room temperature, with a value for the conductivity of about 100 S cm^{-1} in the *ab* plane. We have measured the anisotropy within this plane, and find that this is small, with a higher conductivity in the direction of the *a* axis than in the *b* axis. However, we have available only small crystals so that the electrical contacts made to them cannot be treated as small in relation to the size of the sample in the *ab* plane, and this introduces considerable uncertainty into the determination of the anisotropy, which we made using the Montgomery [30] analysis.

There is a sharp transition to an insulating state at around 56.5 K, defined as the peak value of $\partial \ln \rho / \partial(1/T)$, as shown in figure 9. The transition appears to be sharp, but second-order, with no evidence for any thermal hysteresis. The temperature dependence of the thermopower as measured along the *a* axis is shown in figure 10. In the metallic regime, the thermopower is small and negative, approximately $-7\,\mu$V K^{-1} at 300 K, indicating that the carriers are electron-like. With the Fermi energy in the middle of a single quasi-one-dimensional band, as shown in figure 7, the thermopower is expected to be very small, and its sign is not easy to predict. The transition from metal to semiconductor is clearly seen; the thermopower changes sign and rises to a very much larger value, consistent with the opening up of an energy gap at the Fermi energy.

Under pressure the resistivity in the metallic phase falls, at room temperature to 50% of its ambient pressure value at 7 kbar. Figure 11 shows the temperature dependence of
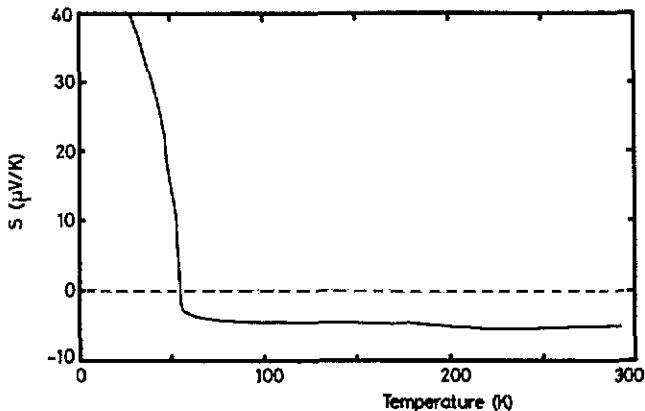

Figure 10. Variation with temperature of the thermopower measured in the *ab* plane.
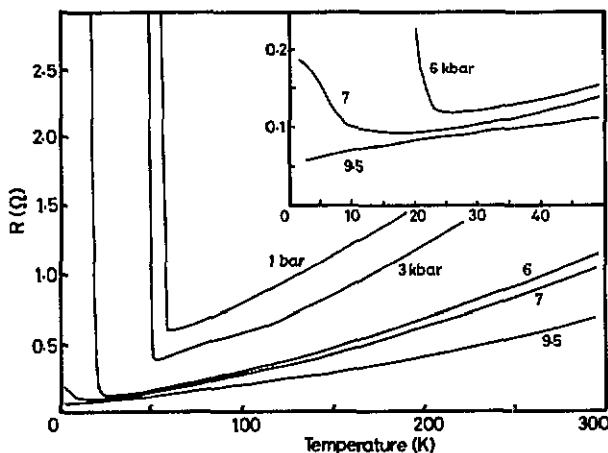
Figure 11. Variation of the resistivity in the *ab* plane at 1 bar and at various values of pressure, indicated in kbar on the figure. Inset shows low-temperature data on an expanded temperature axis.

the resistivity at several pressures. We note that the metal–insulator transition is pushed to lower temperatures, and that the resistivity in the insulating phase remains lower as the pressure is increased. Figures 12 and 13 show the variation of the transition temperature T_p and the activation energy for conductivity E_g, below the transition as a function of pressure. T_p was defined as the temperature at the peak value of $\partial \ln \rho / \partial (1/T)$ and E_g was taken from fitting the resistivity below the transition to $\rho = \rho_0 \exp(E_g/kT)$ in the temperature range a few kelvins below the transition. It is clear that the transition to the insulating state is readily suppressed under pressure, with both T_p and E_g falling towards zero. However, we note that though E_g falls to zero at 6 kbar, the resistivity at higher pressures can still show an upturn at low temperatures. This is clearly seen in figure 11 for the data at 7 kbar, and we consider that there is still a transition at this pressure, though no longer to an insulating state, but rather to a semimetallic state. We discuss later how this may be related to the presence in the
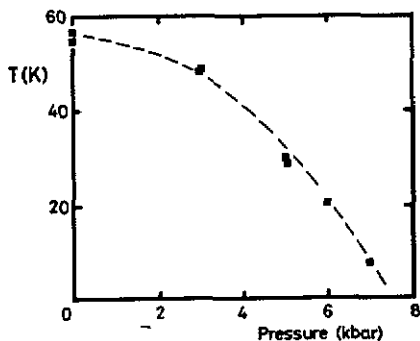

Figure 12. Variation with pressure of the metal-to-insulator transition temperature T_p defined by peak value in $\partial \ln \rho / \partial T$, except at 7 kbar where the transition is taken at the upturn in the resistivity.
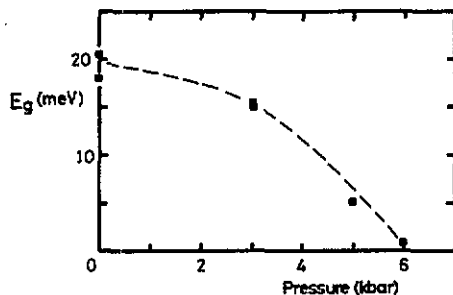

Figure 13. Variation with pressure of the conductivity activation energy E_g, in the insulating phase.

insulating phase of two distinct modulations in the low-pressure regime. At pressures higher than this we have found that the resistivity can fall monotonically with falling temperature, as shown in figure 11 at 9 kbar. However, this is dependent on sample condition, and we have found slight upturns in resistivity for other samples even at pressures of up to 20 kbar. We suspect that this upturn is due to a current distribution that includes a component in the high-resistivity direction perpendicular to the molecular sheets, and is therefore extrinsic in origin. We saw no evidence for superconductivity at pressures up to 20 kbar and temperatures down to 1.4 K.

We take the magnetic susceptibility χ to be of the form

$$\chi = \chi_{core} + \chi_{Pauli} + C/T. \tag{1}$$

The value of C is obtained from the low-temperature variation of χ, and we obtain here a value of $C = 42 \times 10^{-3}$ emu K mol^{-1}. If this is due to spin $\frac{1}{2}$ impurities, this is equivalent to 1.1% per formula unit. This is a high value for an impurity spin concentration, though not exceptional among organic charge-transfer salts of this type. The contribution to χ_{core} from the diamagnetic susceptibility of the ions can be estimated from Pascal's constants [31], and we estimate a value of -87.5×10^{-6} emu mol^{-1} for the dmit group and a total value of -417×10^{-6} emu mol^{-1} for Cs[Pd(dmit)$_2$]$_2$. We did perform a direct measurement of the core susceptibility for the insulating salt (TEA)$_2$[Zn(dmit)$_2$] (TEA = triethylammonium), from which we calculate a value of $-64 \pm 4 \times 10^{-6}$ emu mol^{-1} for the dmit group, after subtraction of the contributions for the zinc and TEA. This value is close to the calculated value, and gives us confidence that the values that we are using for the delocalized π-electron system in the anion are reasonable. The temperature dependence of the remaining contribution to χ, that due to the delocalized metallic electrons and labelled as χ_{Pauli} in equation (1), is shown in figure 14. In the metallic regime, above the metal-to-insulator transition, the susceptibility is independent of temperature, and has rather a high paramagnetic value. At the transition, χ falls abruptly, dropping by 370×10^{-6} emu mol^{-1} between 58 and 55 K, and remaining independent of temperature below this. We consider that χ_{Pauli} drops to zero in the low-temperature phase, and have therefore used a value for χ_{core} of -460×10^{-6} emu mol^{-1}, which is chosen to bring χ_{Pauli} to zero in this temperature regime. This is close to the value calculated from Pascal's constants due to the diamagnetic susceptibility, and we
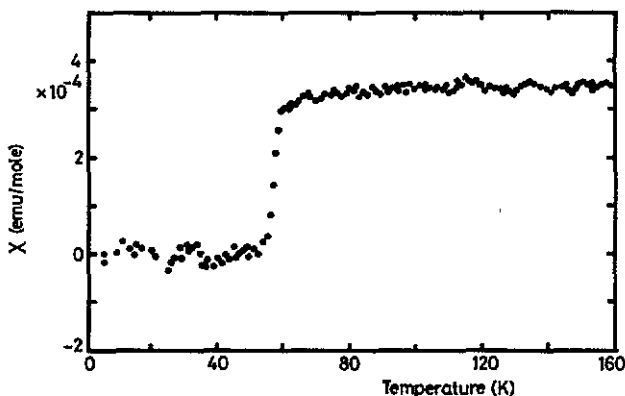

Figure 14. Variation with temperature of the magnetic susceptibility χ_{Pauli} obtained from the measured value of χ by subtraction of the Curie tail due to localized magnetic impurities and subtraction of the diamagnetic core susceptibility (-460×10^{-6} emu mol^{-1}).

attribute the difference between the two values to other contributions to χ_{core} such as Van Vleck paramagnetism.

As presented in section 7, x-ray measurements indicate that the metal–insulator transition is associated with the setting-up of two modulations. We do not have evidence from the conductivity, thermopower or susceptibility data for two distinguishable phase transitions. We note that the transition temperature defined by the peak slope of ρ, S or χ with respect to temperature is found to be close to 56.5 K, though there is evidence for 'pretransitional' changes in these quantities up to 10 K above this temperature.

6. Optical reflectivity

6.1. Experimental details

Reflectance spectra were measured by use of an Olympus MMSP microspectrophotometer from 4200 to 25 000 cm⁻¹, and a Jasco MIR 300 microspectrophotometer in the range 450 to 4200 cm⁻¹. Temperature control was achieved by use of a closed-cycle cryogenic refrigerator manufactured by CTi Spectrim for measurements in the visible part of the spectrum, and by use of an Oxford Instruments continuous-flow cryostat in the infrared. Details of the apparatus have been described previously [32, 33].

6.2. Results

The temperature dependence of the reflectance spectra for light polarized parallel to the a axis and parallel to the b axis is shown in figures 15(a) and (b). The reflectance spectra shows three main features. These are the Drude-like dispersion below 3000 cm⁻¹ associated with the free carriers, weak dispersion at about 4000 cm⁻¹ and strong dispersion at around 11 000 cm⁻¹. The free-carrier dispersion is fairly isotropic within the ab plane, and its changes below the phase transition are consistent with the opening of an energy gap in the low-temperature phase. The dispersion around 4000 cm⁻¹ is observed only in the spectrum for polarization parallel to a, and its form varies with temperature. The feature at higher energy is strongly polarized along the a axis, and splits into two bands below the phase transition temperature. We have analysed the reflectance spectra by fitting to a Drude–Lorentz model, taking the complex dielectric function $\varepsilon(\omega)$ to be of the form

$$\varepsilon(\omega) = \varepsilon_0 - \omega_p^2/(\omega^2 + i\gamma\omega) - \sum_j \Omega_{pj}^2/(\omega^2 - \omega_j^2 + i\Gamma_j\omega) \qquad (2)$$

where ε_0, ω_p, γ and $[\omega_j, \Omega_{pj}, \Gamma_j]$ denote the background dielectric constant, the plasma frequency of the intra-band transition, the relaxation rate of the free carriers, and the parameters of the Lorentz oscillator for the jth excitation respectively. In this curve-fitting procedure we neglect the dispersion around 4000 cm⁻¹ since this feature is small and the lineshape could not be well reproduced by the Lorentz function. The values obtained for the plasma frequencies are 6000 cm⁻¹ (parallel to a) and 6200 cm⁻¹ (parallel to b) at 80 K. From these plasma frequencies, the values of the optical mass, which is an average of the effective masses of all electrons in the conduction band, are calculated to be $3.0m_e$ (parallel to a) and $2.8m_e$ (parallel to b) assuming one conduction electron per dimer. These values show that the carriers can move freely in the ab plane and indicate that the Fermi surface may be rather more isotropic than apparent from the calculations presented in section 4. It is possible that this arises from the closing of the Fermi surface
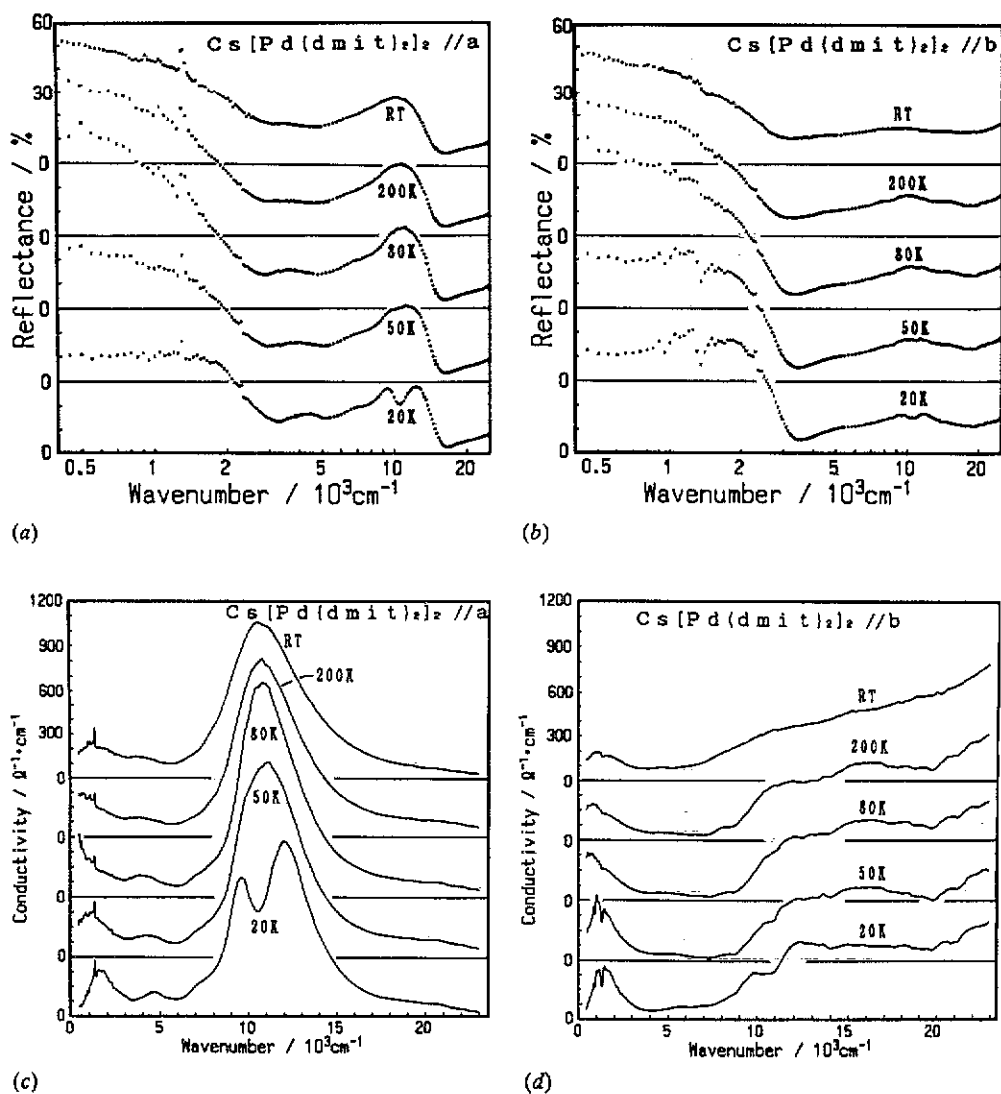
Figure 15. Reflectance versus wavenumber for light polarized (a) parallel to the a axis and (b) parallel to the b axis of Cs[Pd(dmit)$_2$]$_2$ measured at the temperatures indicated. Note the scale offset between the different temperature runs. (c), (d) The optical conductivities parallel to the a and b axes, respectively, obtained by Kramers–Kronig analysis of the data shown in (a) and (b).

through the raising of the conduction band minimum at X through the Fermi level. Full discussion of this issue is deferred to section 8.

The broad dispersion at around 11 000 cm^{-1} is the most characteristic feature in the spectrum of the material. A similar dispersion is also seen in the isostructural AsMe$_4$[Pd(dmit)$_2$]$_2$, though not in the isostructural NMe$_4$[Pd(dmit)$_2$]$_2$ [34]. This band splits below the phase transition temperature. The intensity of this dispersion was estimated by two methods, the first being that described above. We fit to two Lorentz oscillators for the broad dispersion seen for polarization parallel to the a axis. The sum

of the intensity parameters for the two Lorentz oscillators $\Sigma\Omega^2_{pj}$ is 250 (room temperature), 274 (200 K) and 322 (80 K) (in units of 10^6 cm^{-1}), respectively, for each temperature. The second method is based on the Kramers–Kronig transformation. Figures 15(*c*) and (*d*) show the conductivity spectra obtained by the transformation from the reflectance spectra of figures 15(*a*) and (*b*). The intensity of this broad band was estimated directly by integrating the $E_{\|a}$ conductivity spectrum from 6000 to 16 000 cm^{-1}. The values of the intensity parameters thus obtained are 213 (room temperature), 221 (200 K), 239 (80 K), 238 (50 K) and 227 (20 K) (in units of 10^6 cm^{-1}), respectively. The intensity parameters obtained by the two different methods are in good agreement.

We assign this feature to an intermolecular charge-transfer (CT) transition, although the intensity of the 11 000 cm^{-1} feature is very large for such a transition. In the present case in which the dimerization amplitude is large, the Ψ^-_{HOMO} is calculated to lie above the Ψ^+_{LUMO}, so that the Ψ^-_{HOMO} is half-occupied. Thus there are five possible optical transitions: $\Psi^+_{\text{HOMO}} \rightarrow \Psi^-_{\text{HOMO}}$, $\Psi^+_{\text{HOMO}} \rightarrow \Psi^-_{\text{LUMO}}$, $\Psi^+_{\text{LUMO}} \rightarrow \Psi^-_{\text{HOMO}}$, $\Psi^+_{\text{LUMO}} \rightarrow \Psi^-_{\text{LUMO}}$ and $\Psi^+_{\text{HOMO}} \rightarrow \Psi^-_{\text{LUMO}}$. Among these, only two transitions, $\Psi^+_{\text{LUMO}} \rightarrow \Psi^-_{\text{LUMO}}$ and $\Psi^+_{\text{HOMO}} \rightarrow \Psi^-_{\text{HOMO}}$, are expected to have a large intensity, since the intra-dimer transfer integrals between HOMO and LUMO are larger than other integrals because the eclipsed molecular overlap is strong. Thus, these two transitions are the most likely candidates for the strong peak at 11 000 cm^{-1}. Since the energy differences between Ψ^+_{LUMO} and Ψ^-_{LUMO} and between Ψ^+_{HOMO} and Ψ^-_{HOMO} are almost equal, as shown in figure 6, the two electrons filling the Ψ^+_{LUMO} and the one hole in the Ψ^-_{HOMO} dimer are expected to give transitions at almost the same energy. If we assign the dispersion at 11 000 cm^{-1} to the superposition of these two transitions, the value of $2t$ (twice the value of the intra-dimer transfer integral) is then set at 1.4 eV (= 11 000 cm^{-1}). Within the dimer model the intensity parameter for the $\Psi^+_{\text{HOMO}} \rightarrow \Psi^-_{\text{HOMO}}$ transition can be expressed as $\Omega^2_p = 4\pi e^2 d^2 t / V \hbar^2$, where V is the volume of the dimer and d is the a-axis component of the spacing of the dimer. This relation gives a value of 72×10^6 cm^{-1} when we take a value of $t = 0.7$ eV. The $\Psi^+_{\text{LUMO}} \rightarrow \Psi^-_{\text{LUMO}}$ transition is twice this value, so that we estimate a total intensity of 312×10^6 cm^{-1}, which is consistent with the experimental values. In this calculation, we use the Pd–Pd distance for the spacing of the dimer. If we use instead the distance between the molecular centres, the calculated total intensity parameter increases by 20%. According to this assignment, the splitting of this dispersion below the temperature of the phase transition is due to the change in the intra-dimer transfer integrals.

Two other excitations, $\Psi^+_{\text{LUMO}} \rightarrow \Psi^-_{\text{HOMO}}$ and $\Psi^-_{\text{HOMO}} \rightarrow \Psi^-_{\text{LUMO}}$ are expected to appear weakly in the optical spectra because of the small overlaps between HOMO and LUMO of the adjacent molecules. From the solution spectrum of [Pd(dmit)₂]$^-$ we have estimated the energy difference between HOMO and LUMO to be about 0.9 eV (which is somewhat larger than the values calculated here). Assuming this value together with the intra-dimer transfer integrals, which we have already discussed, the peak at 4000 cm^{-1} is assigned to the $\Psi^+_{\text{LUMO}} \rightarrow \Psi^-_{\text{HOMO}}$ transition, and the shoulder at 8000 cm^{-1} to the $\Psi^-_{\text{HOMO}} \rightarrow \Psi^-_{\text{LUMO}}$ transition.

7. Diffuse x-ray scattering

7.1. Experimental details

As in previous studies of structural instabilities of organic conductors, the experiment has been performed with the so-called fixed film–fixed crystal method, using a mono-

chromatized Cu K_α x-ray source as incident radiation. Temperatures regulated in the range 23 K to room temperature were obtained with a closed-circuit cryostat. The photographic study was completed by quantitative intensity measurements using a position-sensitive linear detector.

7.2. Results

Evidence for a low-temperature structural distortion is seen by comparison of the x-ray scattering patterns taken at about 30 K (figure 16(a)) and at about 65 K (figure 16(b)). Figure 16(a) shows supplementary Bragg reflections, with two types of intense satellite reflections present below 56.5 K:

(i) Incommensurate superlattice spots (identified with black arrows in figure 16(a)), which can be indexed by the reduced wavevector $q_1 = (1, \frac{1}{2}(1 - \delta), 0)$ with respect to the main Bragg reflections of the high-temperature C-centred monoclinic lattice. The deviation from the commensurate wavevector $(1, \frac{1}{2}, 0)$ is very small, with δ equal to about 0.04, and this value does not vary significantly with temperature between 56.5 K and the lower limit of these experiments of 23 K.

(ii) Commensurate Bragg reflections (identified with white arrows in figure 16(a)), at the reduced wavevector $q_B = (1, 0, 0)$. These break the C centring monoclinic symmetry of the high-temperature structure.
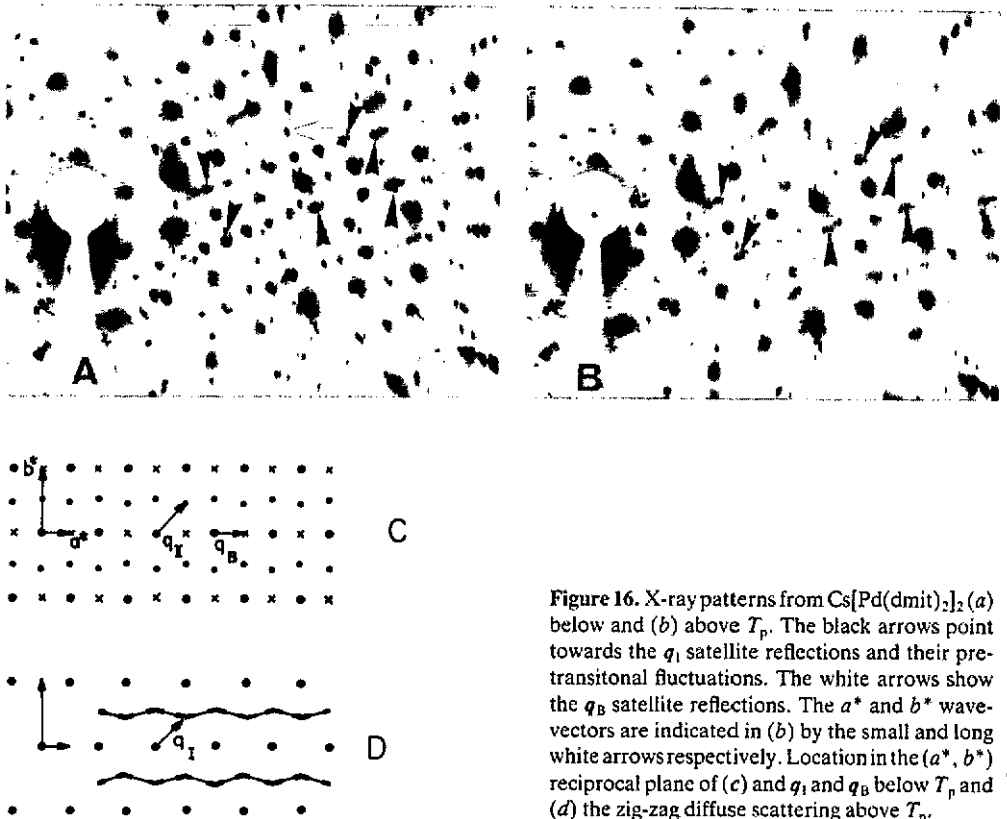
Figure 16. X-ray patterns from $Cs[Pd(dmit)_2]_2$ (a) below and (b) above T_p. The black arrows point towards the q_1 satellite reflections and their pre-transitonal fluctuations. The white arrows show the q_B satellite reflections. The a^* and b^* wavevectors are indicated in (b) by the small and long white arrows respectively. Location in the (a^*, b^*) reciprocal plane of (c) and q_1 and q_B below T_p and (d) the zig-zag diffuse scattering above T_p.

Figure 17. Temperature dependence of the intensity of a q_I incommensurate satellite reflection, shown for both cooling and warming.

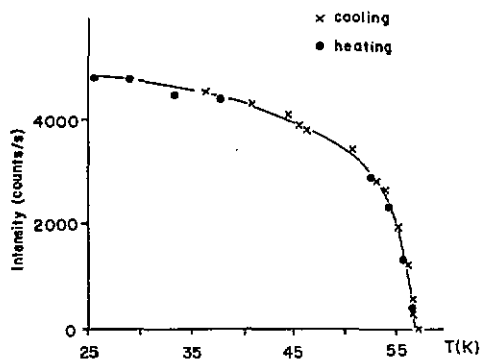Pretransitional fluctuations are seen only for the incommensurate satellite reflections, and these can be detected up to 100 K. These fluctuations have a zig-zag shape joining the reciprocal wavevectors $q_I = (1, \frac{1}{2}(1 - \delta), 0)$ along a^*, with a value of δ of about 0.1 for the x-ray pattern shown in figure 16(b).

Figure 17 shows the temperature dependence of an incommensurate satellite reflection for a heating and a cooling cycle. The satellite intensity extrapolates to zero at $T_p = 56.5 \pm 1$ K. Note that the increase in satellite intensity observed just below T_p is very rapid. Neverthertheless, the photographic study seems to indicate that the intensity really vanishes at a temperature T_c, a few degrees above T_p. Within experimental uncertainties no hysteresis was observed between the heating and warming curves, and the structural transition thus appears to be continuous (second-order). The shift of δ from 0.1 to 0.04 apparently occurs in a very narrow temperature range of less than 4 K around T_p. The photographic study shows that the Bragg reflections associated with the q_B commensurate superlattice vanish at about T_p.

We show in the appendix how the primary (incommensurate) and secondary (commensurate) superstructures can be coupled within Landau theory, and we note that the two superstructures should set in at different temperatures: T_c for the primary and T_2 for the secondary distortion. Experiment shows that the two transitions must be very close together, but we have some evidence that there is condensation of the diffuse scattering associated with the primary distortion at a temperature near 60 K ($= T_c$), and that the transition at 56.5 K, which is much more clearly identified from the transport properties and in the x-ray measurements, is associated with the setting-up of the secondary distortion, T_2, together with a sharp increase in the strength of the primary distortion whose extrapolation at zero occurs at T_1. At the present stage of our investigation, it seems that T_1, T_2 and T_p are all very close together. However, further experiments are in progress to investigate the temperature range close to T_p.

8. Discussion

Cs[Pd(dmit)₂]₂ provides a wide range of phenomena of interest, most strikingly the complicated coupling of two structural transitions to give the low-temperature insulating ground state. We also have considerable information about metallic state properties of this material, and we can hope to gain a rather detailed description of its electronic properties.

Below 56.5 K $Cs[Pd(dmit)_2]_2$ exhibits a structural distortion (section 7) with an energy gap at the Fermi level, as seen in measurements of the electrical conductivity, thermopower and magnetic susceptibility (see section 5), and in the optical properties (section 6). The observation of a metal-to-insulator transition accompanied by a structural distortion suggests that $Cs[Pd(dmit)_2]_2$ undergoes a Peierls-like transition, in which at least part of the energy of stabilization of the distorted state is due to the gapping of large parts of the Fermi surface through the introduction of a hybridization gap for the sections of Fermi surface nested by an incommensurate wavevector. There is strong support for this in: (i) the match between the measured value of q_1 and the wavevectors calculated to nest the Fermi surface, q_1 and q_s (see section 4); (ii) since q_1 and q_2 are close, a unique distortion can give simultaneously reasonable nesting of the Fermi surfaces associated with each of the two slabs; and (iii) the zig-zag shape of the pretransitional fluctuations can be accounted for by the nesting of the one-dimensional portions of the Fermi surface, which are tilted with respect to the b^* direction. There are, however, structural features that indicate that the mechanism for the transition is more complex than that of a classical Peierls transition:

(i) Additional Bragg reflections are seen below T_p with a commensurate wavevector q_B that cannot be considered as a second harmonic $2q_1$, of the incommensurate modulation.

(ii) The pretransitional fluctuations and the structural distortion do not occur at exactly the same wavevector: δ shifts sizably around T_p.

Clearly the structural transition of $Cs[Pd(dmit)_2]_2$ involves two components of the distortion that have different symmetry of translation. These are described by an incommensurate order parameter (the primary order parameter), which corresponds to the structural distortion associated with the CDW instability and shows pretransitional fluctuations, and a commensurate order parameter (the secondary order parameter), which describes the breaking of the C centring symmetry and does not show pretransitional fluctuations. Translational symmetry allows a biquadratic coupling between these two order parameters. This coupling must be attractive in order to stabilize a secondary distortion. However, with such a coupling, an elementary Landau theory predicts two phase transitions (see appendix): the upper one at T_c associated with the development of the primary order parameter and a further transition at a lower temperature associated with the onset of the secondary order parameter at T_p.

It is evident that the nature of the superlattice structure, with two modulations with different symmetries of translation, does not fall within the standard description of a Peierls transition, and that we need to consider carefully the nature of the electronic structure of this material in both the metallic and insulating states. The first puzzle is that though there is clearly strong gapping over the whole Fermi surface, the electronic structure is calculated to be two- rather than one-dimensional (see figure 7), and it would be expected within a conventional weak-coupling model for the Peierls instability of the coupled lattice–electron gas that the gapping of the Fermi surface produced by the superlattice would be incomplete, giving a transition from metal to semimetal.

The transport and optical data presented in sections 5 and 6 do in fact provide clear evidence that the modification of the electronic structure in the vicinity of the Fermi energy is much stronger than would be expected for a Peierls transition setting in at 56.6 K, as we outline below. Within the weak-coupling model for the Peierls distortion in a one-dimensional system, the gap at $T = 0$, $2\Delta(0)$ is related to the mean-field transition temperature T_p by $2\Delta(0) = 3.5k_B T_c$ [35]. (Note that we do not expect to see

strong one-dimensional fluctuations, which might depress the transition temperature below its mean-field value, as there is ample experimental evidence for rather strong two-dimensional coupling within the anion sheets.) We can relate the size of the gap to the measured conductivity below the transition. Assuming conduction through thermal excitation of electron–hole pairs across the gap, E_g is equated with half the gap Δ, and with $T_p = 56.5$ K we expect a value for E_g of 8 meV. The experimentally measured value of E_g is very considerably larger than this; the measured value at ambient pressure is about 20 meV (see figure 13). The loss of the Pauli contribution to the magnetic susceptibility below the transition is extremely sharp; the data shown in figure 14 show a drop to essentially zero within 6 K of the transition temperature. This again is indicative of the opening of a large gap for the magnetic excitations. The optical reflectivity data shown in figure 15 show modification below the transition temperature on an even larger energy scale. There is partial loss of the Drude reflectivity up to 1500 cm^{-1} (186 meV), and a splitting in the structure near 10 000 cm^{-1} associated with transitions from Ψ_{HOMO}^{+} to Ψ_{HOMO}^{-} and from Ψ_{LUMO}^{+} to Ψ_{LUMO}^{-} of 2300 cm^{-1}.

These energies are considerably larger than the gap energy deduced from the conductivity data, and give very clear evidence that the structural distortions associated with the metal–insulator transition are of large amplitude, affecting states throughout the conduction band, and cannot be simply related to the details of the band structure in the vicinity of Fermi energy. In this situation the relevance of details of Fermi surface nesting to the periodicity of the superlattice set up may seem to be rather slight. We consider that the superlattices set up in some of the transition-metal dichalcogenides, such as the 1T and 2H polytypes of TaS$_2$ and TaSe$_2$, may provide useful comparison in that these materials for which Fermi surface nesting does appear to fix the superlattice although the distortion amplitude is again large [35]. In this context we note that the biquadratic term that couples the primary and secondary order parameters in the Landau theory presented in the appendix depends for its effectiveness on the strength of the two distortions, and we consider that it is no coincidence that this coupling of the two distortions is seen in a system that exhibits such a strong distortion amplitude.

Let us now consider possible mechanisms that may give rise to the secondary distortion. This distortion could be induced by a change of the intra-layer CDW stabilizing energy or by coupling between the CDW on adjacent layers. The observed shift of δ shows that the secondary distortion is more likely to result from the former. A possible mechanism is as follows. Without the secondary distortion, the nesting of the Fermi surface is not perfect and the CDW distortion leads to the formation of small pockets of carriers, with one carrier type on one side of the Brillouin zone (in the direction of X) and the other carrier type on the other side, as shown schematically in figure 18(*a*). In the presence of the secondary distortion, with wavevector q_B, new Brillouin zone boundaries perpendicular to ΓX appear at $\pm a^*/2$ (i.e. at ΓX/2 in figure 8). Since the electron and hole pockets are in the vicinity of these new zone boundaries, we can expect that there will be substantial hybridization of the two carrier pockets, and we can expect quite generally to see the opening of a gap between the 'bonding' and 'antibonding' combinations of these hybrids. This is illustrated schematically in figure 18(*b*), and can result in a transition from a semimetallic band structure in the presence of only the primary distortion to an insulating band structure when the secondary distortion is additionally present. The driving force therefore for the secondary distortion is the reduction in band energy represented by the formation of the hybridization gap shown in figure 18(*b*).

We comment here on the apparent discrepancy between the band-structure cal-
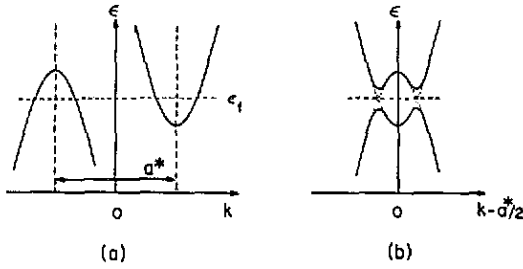
Figure 18. (*a*) Schematic representation of the electron and hole pockets resulting from the nesting of the Fermi surface shown in figure 8 by q_1. (*b*) Hybridization of these pockets by the secondary distortion of wavevector a^*.

culation of section 4, which gives an open Fermi surface, and the optical data of section 6, which shows an almost isotropic plasma frequency within the *ab* plane, indicating that the electronic motion is effectively isotropic within the *ab* plane. Using the Fermi sheets of figure 8(*a*) the ratio between the plasma frequencies parallel to *b* and *a* can be estimated to be about 1.75. The optical measurements of section 6 give a ratio close to 1. We have previously suggested that small modifications to the band dispersion presented in section 4 might result in the closing of the Fermi surface, and thus in a reduction of the anisotropy of the electronic structure in the *ab* plane. This three-dimensional Fermi surface could then lead to an almost isotropic ratio of plasma frequencies and conductivities, but since large portions of this surface have been left practically unaltered from those discussed in section 4, there may still be effective nesting of the Fermi surface. This still provides the driving force for the primary distortion observed in diffuse x-ray scattering experiments.

The high-pressure phase diagram is evident in figures 12 and 13, and it is seen that the phase transition (or transitions) is (are) readily pushed to lower temperatures under quite modest pressures. The activation energy for conductivity broadly tracks with the transition temperature, as expected for the simple Peierls distortion, though here we must regard this as accidental. It seems that all trace of the phase transitions as detected in the resistivity is suppressed at 9 kbar, but we note that the data shown in figure 11 show a distinct change in form between 6 and 7 kbar. At the lower pressure the transition is to a semiconducting state, with a well defined energy gap, and we would consider that, as at ambient pressure, both primary and secondary superlattices are present. At 7 kbar, however, we see a distinct phase transition, at 8 K, but though the resistivity below it rises, it remains metallic. We speculate here that this may be due to a separation of the two phase transitions, with only the primary superlattice present at this pressure. Within the model that we have outlined above this would then give incomplete gapping of the Fermi surface, and a transition to a semimetallic state. In view of the large modifications of the band energies brought about by the superstructures, up to 0.2 eV as seen in the optical measurements, it is surprising that pressure can so quickly drive them out; we can offer no simple explanation for this.

We can use the presence of the metal–insulator transition to give a useful calibration of the magnetic susceptibility of this material, so that we can with confidence decompose the measured susceptibility into components associated with the conduction electrons and those due to the ion cores. The magnitude of the susceptibility attributable to the conduction electrons can be accurately gauged from the jump in the value of the

susceptibility at the metal-to-insulator transition. We measure a value of 3.7×10^{-4} emu mol^{-1} formula unit for this. We can compare this with the value expected from the Pauli susceptibility of the conduction electrons, $\chi_{\text{Pauli}} = N_A \mu_B^2 N(E_F)$, where $N(E_F)$ is the density of states at the Fermi energy. For the situation where the Fermi energy lies in the middle of the band shown in figure 7, the value of $N(E_F)$ may depend sensitively on the proximity of the Van Hove singularity at X. If we take the case where it is not close to the Fermi energy, then we calculate a value close to 2×10^{-4} emu mol^{-1} for both a one-dimensional and a two-dimensional dispersion, taking the bandwidths shown in figure 7, which were calculated for the single-ζ basis. This value is almost a factor of 2 smaller than the measured value. If the true bandwidths are, as seems likely, larger than this, as calculated with the double-ζ basis set, then the discrepancy is even larger. This may be in part due to the Van Hove singularity, but it seems very likely that the experimental value for the conduction electron susceptibility is higher than the calculated value, as is commonly observed for molecular metals of this type, and we consider that there is enhancement of the electron susceptibility due to electron correlations.

9. Conclusions

We find that Cs[Pd(dmit)₂]₂ is a molecular metal of considerable interest, and that, though we have presented a detailed study of a wide range of physical properties together with band calculations, there remains much to be done. The detailed modelling of the bands in the vicinity of the Fermi energy and the determination of the dimensionality of the electron system is not fully resolved. X-ray measurements are in progress to investigate further the coupling of the primary and secondary distortions, and the differentiation of the two phase transitions expected from the formation of these two modulations of the lattice.

Appendix

The simplest Landau free-energy development that includes a biquadratic attractive coupling ($\mu > 0$) between a primary order parameter ψ and a secondary distortion φ is

$$F = \tfrac{1}{2}a(T - T_c)\psi^2 + \tfrac{1}{4}B\psi^4 - \tfrac{1}{2}\mu\varphi^2\psi^2 + \tfrac{1}{2}K\varphi^2 + \tfrac{1}{4}L\varphi^4.$$

It leads to a second-order phase transition at T_c, below which

$$\psi^2 = a(T_c - T)/B \qquad \text{and} \qquad \varphi = 0.$$

If $\mu\psi^2 > K$, then there will be a further phase transition at a lower temperature to set up finite amplitude in the secondary order parameter φ. This transition is second-order if $r^2 \equiv \mu^2/BL < 1$. It occurs if $r > s \equiv (K/aT_c)(B/L)^{1/2}$ at critical temperature $T_2 = T_c(1 - s/r)$. Below T_2 we have

$$\varphi^2 = \frac{ar^2}{\mu}\frac{(T_2 - T)}{1 - r^2} \qquad \text{and} \qquad \psi^2 = \frac{a}{B}\frac{(T_1 - T)}{1 - r^2} \qquad \text{with} \qquad T_1 = T_c(1 - sr).$$

Since $r < 1$ we have $T_2 < T_1 < T_c$. As μ gets larger, T_2 tends towards T_1 and the two merge in a tricritical point for $r = 1$. For larger values of μ the transition becomes first-order and its analysis requires consideration of higher-order terms in the free-energy expansion. Here s is the geometric mean of the relative shifts of T_1 and T_2 with respect

to T_c. In the case of $Cs[Pd(dmit)_2]_2$, T_1 and T_2 are very close to one another, $T_1 \sim T_2 \sim T_p$, with T_c a few degrees above this. This suggests that $r \sim 1$ and the $s \ll 1$. The first feature means that the coupling μ between the two distortions is quite large, and the second feature means that the force constant K associated with the secondary distortion is particularly soft.

References

[1] Brossard L, Ribault M, Bousseau M, Valade L and Cassoux P 1986 *C. R. Acad. Sci. Paris* **302** 205
[2] Brossard L, Ribault M, Valade L and Cassoux P 1986 *Physica* B **143** 378
[3] Schirber J E, Overmyer D L, Williams J W, Wang H H, Valade L and Cassoux P 1987 *Phys. Lett.* A **120** 87
[4] Brossard L, Ribault M, Valade L, Legros J-P and Cassoux P 1988 *Synth. Met.* **27** B157
[5] Brossard L, Ribault M, Valade L and Cassoux P 1989 *J. Physique* **50** 1521
[6] Kobayashi A, Kato R and Kobayashi H 1987 *Synth. Met.* **19** 635
[7] Kobayashi H, Kato R, Kobayashi A and Sasaki Y 1985 *Chem. Lett.* 191
[8] Kobayashi A, Sasaki Y, Kato R and Kobayashi H 1986 *Chem. Lett.* 387
[9] Kato R, Kobayashi H, Kobayashi A and Sasaki Y 1985 *Chem. Lett.* 131
[10] Kobayashi A, Kim H, Sasaki Y, Moriyama S, Nishio Y, Kajita K, Sasaki W, Kato R and Kobayashi H 1988 *Synth. Met.* **27** B339
[11] Kim H, Kobayashi A, Sasaki Y, Kato R and Kobayashi H 1987 *Chem. Lett.* 1799
[12] Kato R, Mori T, Kobayashi A, Sasaki Y and Kobayashi H 1984 *Chem. Lett.* 1
[13] Underhill A E, Varma K S, Clark R A and Underhill C E 1990 *Springer Proc. Phys.* **51** 412
[14] Kobayashi A, Kim H, Sasaki Y, Kato R, Kobayashi H, Moriyama S, Nishio Y, Kajita K and Sasaki W 1987 *Chem. Lett.* 1819
[15] Kajita K, Nishio Y, Moriyama S, Kato R, Kobayashi H, Sasaki W, Kobayashi A, Kim H and Sasaki Y 1988 *Solid State Commun.* **65** 361
[16] Clarke R A and Underhill A E 1988 *Synth. Met.* **27** B515
[17] Kobayashi A, Kim H, Sasaki Y, Kato R and Kobayashi H 1987 *Solid State Commun.* **62** 57
[18] Canadell E, Rachidi I E-I, Ravy S, Pouget J-P, Brossard L and Legros J P 1989 *J. Physique* **50** 2967
[19] Ravy S, Pouget J P, Valade L and Legros J P 1989 *Europhys. Lett.* **9** 391
[20] Ravy S (unpublished results)
[21] Clemenson P I, Underhill A E, Hursthouse M B and Short R L 1988 *J. Chem. Soc., Dalton Trans.* 1689
[22] Whangbo M-H and Hoffmann R 1978 *J. Am. Chem. Soc.* **100** 6093
[23] Hoffmann R 1963 *J. Chem. Phys.* **39** 1397
[24] Ammeter J H, Bürgi H B, Thibault J and Hoffmann R 1978 *J. Am. Chem. Soc.* **100** 3686
[25] Canadell E, Ravy S, Pouget J P and Brossard L 1990 *Solid State Commun.* **25** 633
[26] Grant P M 1982 *Phys. Rev.* B **26** 6888
[27] Clementi E and Roetti C 1974 *At. Nucl. Data Tables* **14** 177
[28] Friend R H and Bett N 1980 *J. Phys. E: Sci. Instrum.* **13** 294
[29] Guy D R P and Friend R H 1986 *J. Phys. E: Sci. Instrum.* **19** 430
[30] Montgomery H C 1971 *J. Appl. Phys.* **42** 2971
[31] Landolt–Börnstein 1984 *Numerical Data and Functional Relationships in Science and Technology* New Series, vol 12, ed K-H Hellwege and O Madelung (Berlin: Springer)
[32] Iyechika Y, Yakushi K and Kuroda H 1980 *Bull. Chem. Soc. Japan* **53** 603
[33] Tajima H, Yakushi K, Kuroda H and Saito G 1984 *Solid State Commun.* **49** 769
[34] Tajima H, Tamura M, Naito T, Kobayashi A, Kuroda H, Kato R, Kobayashi H, Clark R A and Underhill A E 1990 *Mol. Cryst. Liq. Cryst.* **181** 233
[35] Friend R H and Jérôme D 1979 *J. Phys. C: Solid State Phys.* **12** 1441